Missing Wedge Computed Tomography by Iterative Algorithm DIRECTT

Andreas Kupsch*[1], Axel Lange[1], Manfred P. Hentschel[1], Sebastian Lück[2], Volker Schmidt[2], Roman Grothausmann[3,4], André Hilger[3], Ingo Manke[3]

[1] BAM Federal Institute for Materials Research and Testing, 12200 Berlin, Germany
[2] Ulm University, Institute of Stochastics, 86069 Ulm, Germany
[3] HZB Helmholtz-Zentrum Berlin, 14109 Berlin, Germany
[4] Hannover Medical School, Institute for Functional and Applied Anatomy, 30625 Hannover, Germany
* corresponding author: e-mail: andreas.kupsch@bam.de, phone: +49 30 8104 3692

Abstract

A strategy to mitigate typical reconstruction artefacts in missing wedge (MW) computed tomography (CT) is presented. These artefacts appear as elongations of reconstructed details along the mean direction (*i.e.* the symmetry centre of the projections). Although absent in standard CT applications they are most prominent in advanced electron tomography and also in special topics of X-ray and neutron tomography under restricted geometric boundary conditions. We investigate the performance of the DIRECTT algorithm (Direct Iterative Reconstruction of Computed Tomography Trajectories) to reduce the directional artefacts in standard procedures. In order to be sensitive to the anisotropic nature of MW artefacts, we investigate isotropic substructures of metal foam as well as circular disc models. Comparison is drawn to filtered backprojection and algebraic techniques. Reference is made to reconstructions of complete data sets. For the purpose of assessing the reconstruction quality Fourier transforms are employed to visualise the MW directly. Deficient reconstructions of disc models are evaluated by a length-weighted kernel density estimation, which yields the probabilities of boundary orientations. The DIRECTT results are assessed at different signal-to-noise ratios by means of local and integral evaluation parameters.

Keywords: Missing Wedge, Computed Tomography, Electron Tomography, Iterative Reconstruction, Reconstruction Algorithm, Image Morphology

1. Introduction

In several applications of computed tomography (CT) based on electrons (Midgley & Dunin-Borkowski, 2009), X-rays (Stock, 2008), and neutrons (Kardjilov *et al.*, 2011), restrictions due to limited access (*e.g.* extended components, fixed objects), directional opacity, limited sample life time/stability or laminographic set-ups present a challenging reconstruction task. Especially advanced electron tomography has continuously improved the potentials of 3D imaging of nanostructures in molecular and cell biology, but suffers from image artefacts due to the limited sector of accessible projection angles (Midgley & Dunin-Borkowski, 2009; Midgley & Weyland, 2003). Such Missing Wedge (MW) measurements are incomplete data sets with respect to standard requirements of established reconstruction algorithms. The respective reconstructions unavoidably result in improper deposition of material density elements. Typical image artefacts are elongations of the actual shapes along the mean direction of projections (Radermacher, 1988; Kawase *et al.*, 2007), *i.e.*, the spatial resolution becomes anisotropic.

The MW issue has been approached in different ways by focussing on the data collection (measurement), the reconstruction algorithm and the quality assessment.
The reconstruction techniques by Filtered Backprojection (FBP) (Radon, 1917; Kak & Slaney, 1988)and Weighted Backprojection (WBP) (Radermacher, 1988)suffer from

deconvolution of projections by an isotropic point spread function. However, from a current point view, iterative algorithms (such as ART, (Gordon *et al*., 1970)) are considered, in particular SIRT (Simultaneous Iterative Reconstruction Technique) (Gilbert, 1972) and more recently discrete tomography (Batenburg, 2005).The latter exploits some *a priori* information. A particular representative of this class of algorithms is the Discrete Algebraic Reconstruction Technique (DART) (Bals *et al*., 2007; Batenburg *et al*. 2009). Considerable advantages by iterative Total Variation (TV) are reported in order to exploit the sparseness of internal structure boundaries (Sidky *et al*., 2006).A masked SIRT/DART algorithm was successfully applied to very few projections under the MW restriction (Zürner *et al*., 2012).Recently, the combination of WBP and SIRT, W-SIRT, was suggested as a promising approach to attack the MW problem (Wolf *et al*., 2014).

On the other hand, sophisticated measuring schemes have been suggested beyond the conventional uniaxial image acquisition with constant angular increments: the equally-sloped tomography (Lee *et al*., 2008) which employs the pseudo-polar fast Fourier transform (Averbuch *et al*., 2008) and the dual axis tomography (Penczek *et al*., 1995; Arslan *et al*., 2006) together with an appropriate SIRT-based algorithm which alternates between the two axes in each iteration cycle (Tong *et al*.,2006). An approach to find a measure for the anisotropic spatial resolution in the reconstructed data by edge spread functions was given by HeidariMezerji *et al*. (2011).

Electron tomographic data usually suffer from the simultaneous occurrence of multiple restrictions, as there are (partial) opacity, a limited field of view (resulting in the region-of-interest problem), variable angular increments and, as the two main obstacles, very few projections and the MW.Fernandez (2013) gives a comprehensive review of computational methods used for electron tomography from data acquisition to advanced reconstruction methods. Chen *et al*. (2014) evaluated the fidelity of different reconstruction techniques by means of edge profiles and the resolvable distance at the example of tubular objects.

In our study we explore the potentials of reducing MW artefacts by adapted strategies of the DIRECTT (Direct Iterative Reconstruction of Computed Tomography Trajectories) algorithm (Lange *et al*., 2003, 2004, 2006, 2008, 2011). The algorithm has been demonstrated to cope with the multiple restrictions of electron tomographic data (Grothausmann *et al*., 2010, 2011) and for neutron tomography as well (Manke *et al*., 2009, 2010; Kupsch *et al*., 2010; Markötter *et al*., 2012).

In order to illustrate a typical application of MW tomography Fig. 1 compares SIRT (a) and DIRECTT (b) reconstructions of a single slice electron tomogram displaying Ru catalyst particle arrangements on carbon support, where the DIRECTT algorithm reveals more details. Apart from the rather subjective perception of the image differences the respective Fast Fourier Transforms (FFT) in the inserts provide a direct integral measure of the directional distribution of edges and remaining anisotropic details (Smith, 1997). The effect of the MW of projections is represented by the dark sector of the 2D FFT of SIRT (Fig. 1a, inset). In contrast, the FFT of DIRECTT indicates a reduction of the MW artefacts (Fig. 1b, inset).Experimental details and TEM images are given elsewhere (Grothausmann *et al*., 2011).

Here, we apply X-ray (parallel beam) tomography in order to be independent of the multiple perturbing effects in electron tomography. Similar to the angular limitations, the sinogram data are truncated at 120°. Experimental X-ray tomography of metallic foam structures as well as simulated model data of circular pores are investigated due to their sensitivity to anisotropic artefacts within the tomograms. Similar nano scale structures have been successfully visualised by electron tomography (Biermans *et al*., 2010).

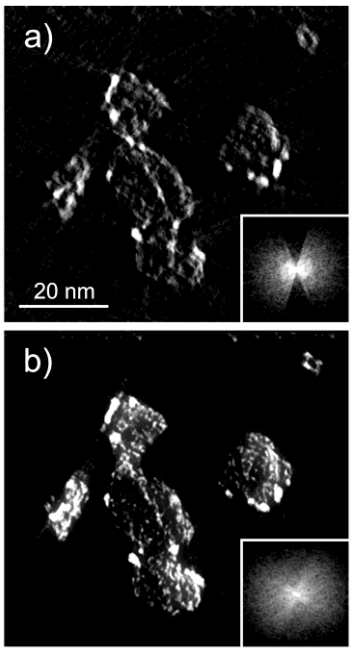

Fig. 1. Illustration of a typical MW tomography application: comparison of electron tomogram slices of Ru catalyst particles on carbon black support and the respective 2D Fourier transform magnitudes (FFT) as insets; (a) SIRT result (pronounced dark FFT sector); (b) DIRECTT reconstruction after 11 iterations (rather isotropic FFT). Projection data were collected in a 143° section of tilt angles with an angular increment of 1° (Grothausmann et al., 2011).

2. DIRECTT Algorithm

The DIRECTT algorithm has been described in detail elsewhere (Lange *et al*., 2004, 2006, 2011). Here, we restrict ourselves to emphasize its key features, which are essential to improve the quality of MW reconstructions.

Like any iterative algorithm DIRECTT is based on a sequence of alternating reconstructions and virtual projections of intermediate reconstruction results, which are subsequently improved. The procedure is illustrated by Fig. 2 at the example of a low resolution pixel model of density singularities in order to image directly single pixel smearing and to monitor their anisotropy under 90° MW conditions. The basic principle of the DIRECTT procedure is the computation of line integrals along sinusoidal traces, which correspond to *each individual* pixel position of the tomogram. Contrary, in FBP sinogram data are "back"-projected into the tomogram.

The following items list distinctive features of the iterative approach:

Initialization

- input of experimental or model attenuation data sinogram
-for *each* pixel within the reconstruction array, assign a weight of the integral along its interpolated (sinusoidal) trajectory within the (optionally filtered) sinogram (Fig. 2c)
- *selection* of predominant reconstruction pixels whose trajectory weight exceeds a pre-defined percentage α of the maximum value occurring in the reconstruction array
- *weighted* summation of the selected pixels to the (empty) reconstruction array by pre-selected factor *f* results in the intermediate reconstruction (Fig. 2h)

Iteration

- projection of the intermediate reconstruction into a temporary sinogram
- subtract the temporary sinogram from the measured one resulting in a "residual sinogram" (difference of projected intermediate reconstruction and original sinogram, Fig. 2i)

- reconstruction of the residual sinogram as before
- weighted summation of the newly selected elements in order to update the intermediate reconstruction array
- repetition of the above steps

Termination

- terminate the algorithm at a pre-defined number of cycles or when the variance or integral weight of the residual sinogram converges, *e.g.* at 99% of the respective initial values (Fig. 2j).

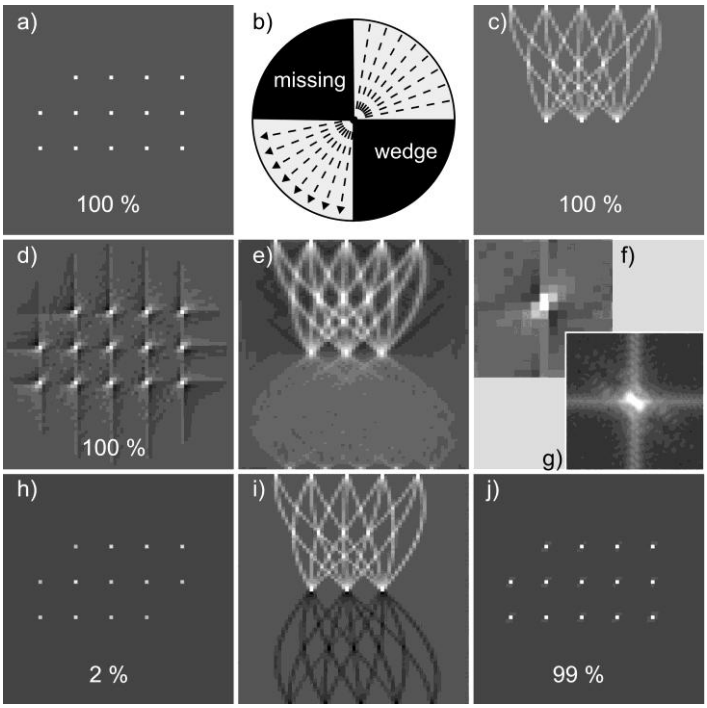

Fig. 2. Principles of iterative model reconstruction under 90° missing wedge conditions by DIRECTT (without filtering); a) 64^2 pixel model containing 14 identical pixels of non-zero mass elements; b) sketch of 90° missing wedge and sector of projections (arrows); c) 180° parallel beam density sinogram of model, 45 projections by 2° and empty missing wedge region below; d) FBP of sinogram (c) (all mass reconstructed); e) sinogram obtained from projecting the FBP reconstruction (d) revealing blurred projections at lower missing wedge half; f) averaged single mass elements of (d) demonstrating typical elongation artefacts; g) magnitude of the Fourier transform (FFT) of elongation artefact of (f) with orthogonal elongation; h) 2% of the total mass selected from unfiltered DIRECTT reconstruction of (c) ($\alpha = 0.8$) revealing a first intermediate reconstruction; i) typical sinogram of intermediate reconstruction according to (h) (after 150 cycles of projections each being subtracted from the original data set of (c)), negative sharp sinogram traces account for the missing wedge; j) DIRECTT reconstruction terminated at 99% retained mass after 300 iteration cycles.

It should be stressed that the selection implies an *update for only a subset* of reconstruction elements in each cycle. The mentioned parameters (weights, selection thresholds, and even filters) can be varied for each cycle either by the operator after assessing the intermediate result (interactive reconstruction) or automatically depending on the iteration progress. The choice of filters depends on the reconstruction task, either to overcome certain restrictions of the measurement (regarding completeness, geometric or intensity distortions) or to emphasize special reconstruction features. The fraction α ranges from 0 (accept all reconstructed values; *i.e.* no selection) to 1 (accept only the maximum absolute value).

High precision of the computed projections results from treating pixels as volume elements of well-defined size and shape instead of points. Given precise projection input, DIRECTT is capable to exceed the resolution of the detector pixel size (Lange *et al.*, 2008).

In addition to the general principles of the DIRECTT procedure, Figure 2 depicts some specific features of a 90° missing wedge of projections (Fig.2b) revealing a limited parallel beam sonogram of the model. Based on 45 projections by 2°steps and the empty missing wedge region in the 180° sinogram (Fig. 2c), the FBP with the total mass reconstructed at once creates the well-known elongation artefacts of the originally single pixel objects at 45°. For better statistical significance all such objects are averaged and magnified in Fig. 2f. In turn, a pronounced perpendicular streak results in their Fourier transform in Fig. 2g. Such anisotropic artefacts do not only result in additionally blurred projections at the lower half of the sinogram (Fig. 2e) of the projected FBP but even in wrong positive density. Fig. 2i accounts for a typical sinogram of an intermediate reconstruction according to h) (after 150 cycles) subtracted from the original sinogram. Negative sharp sinogram traces indicate the missing wedge sector.

In model calculations, DIRECTT has been shown to reduce the MW problem even under severe restrictions (Hentschel *et al.*, 2010). Fig. 3 displays the direct comparison of results computed by DIRECTT and FBP for identical angular sectors of 90, 120 and 180°. While the FBP exhibits dominant elongation artefacts along the mean direction of projection, the iterative procedure reduces those artefacts. The individual images present a pixel model and its reconstructions by FBP and DIRECTT at different MW. The quantification of the elongations is performed by cross section profiles of an individual motif along the mean projection. While for the full data set (180°) Fig. 3d reveals identical FWHM of 14 pixel in both cases, Fig. 3h and 3i result in considerable broadening of the FBP, from 14 to 19 pixel (120° projection) and to 23 pixel (90° projection), respectively.

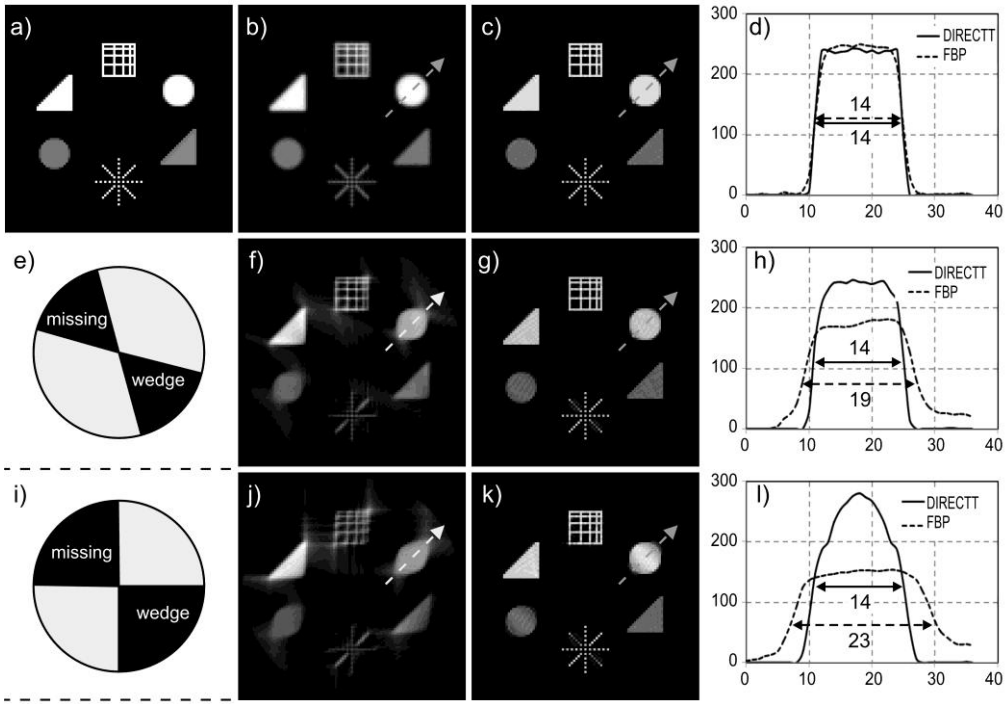

Fig. 3. Missing wedge model calculations: comparison of reconstruction results obtained from FBP and DIRECTT for identical projection sectors of 180°, 120°, and 90° (top to bottom) and quantification of missing wedge elongation artefacts by cross section profiles of the disc motif along the mean direction of projections (dashed arrows); a) 101×101 pixel model; b) 180° FBP; c) 180° DIRECTT reconstruction (α=0.6; 10 iterations, 180 projections); d) cross section plots of disc in (b) and (c) with identical FWHM; e) sketch for 120° projections; f) 120° FBP; g) 120° DIRECTT reconstruction (α=0.8; 50 iterations, 480 projections); d) cross section profiles of disc in (f) and (g) with broadened FWHM of FBP; i) sketch for 90° projections; j) 90° FBP; k) 90° DIRECTT reconstruction (α=0.8; 100 iterations, 360 projections); l) cross section plots of disc in (j) and (k) with broadened FWHM of FBP.

Best results are obtained when the iteration is performed in sufficiently small steps, by choosing α close to unity and a small weighting factor *f*. Thus, very few accepted elements are added to the intermediate reconstruction. The advantage of this strategy is to avoid the early formation of artefacts, which cannot be purged in the further course of iteration. DIRECTT does not leverage *a priori* knowledge at any stage. Moreover, DIRECTT is not similar to SIRT/DART: There is no restriction condition to the pixels to be varied. Neither boundary pixels (DART) nor limited change of grey values (SIRT). Discretisation is not essential, it just helps to accelerate the convergence (see conclusion).

Different computing approaches in C and LabView™ code are implemented but they are not freely available at present. As for all iterative reconstruction techniques, the quality improvements have to be paid by higher computing effort. The number of iteration cycles is roughly a linear factor for extended computing.

3. Partially discrete reconstruction strategy

For the purpose of faster convergence of reconstructions, we modified the standard procedure by a partially discrete reconstruction strategy.

Under the basic assumption of an essentially binary mass distribution, we obtain a rough estimate of the foreground density ρ_0 from the ratio of the integrated mass and the number of non-zero elements (above a threshold) in the initial reconstruction.The procedure is run in three stages. The first two of them rigidly impose binary reconstructions, while the last stage is free of restrictions.

In the first stage, it proves useful to purposely assume a substantially smaller binary value ρ' ($\rho'=\gamma\rho_0$, γ: reduction factor) than estimated from the initial reconstruction. From cycle to cycle the selection threshold α is reduced until the residual sinogram's integral weight converges to a non-zero constant. At the end of stage one, we obtain a reconstruction nearly free of artefacts, but at the purposely chosen small "density" level.

In the second stage, the foreground phase of the intermediate reconstruction is set to the initially estimated value ρ_0 (by multiplication). Iterations are strictly binary (0 and ρ_0), again. Starting from high values α, they are reduced until convergence of the residual sinogram to nearly zero (<1%) is reached. At the end of stage two we obtain an approximate binary solution of the reconstruction.

Stage three, which comprises up to five cycles, is free of restrictions regarding selection and discretisation. The discrete density values are modified continuously in order to approach a non-binary greyscale representation of the true density pattern.

4. Quantitative Assessment

In order to get a measure of the reconstruction quality beyond pure eye inspection, we pursue two approaches of assessment.

At first the remnants of the missing wedge in the reconstruction are assessed as an integral criterion. This is done by evaluating the directional distribution of the magnitudes of the respective Fourier transforms which represent the directional distribution of edges (high frequency components) independent of image details. The directions of the distorted edges of typical elongation artefacts (lacking those components) of isotropic objects correlate directly to the wedge in Fourier space.

The second approach employs spatial statistics to quantify the erroneous elongation of isotropic disc objectsof non-overlapping, randomly positioned pores. The assessment of the reconstruction quality is based on statistical orientation analysis of grey scale gradients of the pore boundaries, followed by thresholding and binarisation. Hence, typical elongation is

reflected by the orientation of these gradients. The extracted phase boundaries are converted to polygonal tracks, *i.e.*, to space continuous vector data (Lück *et al*., 2013). Their directional distribution is investigated by a length-weighted kernel density estimation and is presented by the rose of directions (RDR). Deviations between the extracted boundaries in the phantomsand reconstructions were assessed by the L^2-distance of the density functions.

A general benefit of using simulated phantoms is that in contrast to the reconstruction of experimental projection data, the data to be reconstructed as well as the reconstruction conditions such as signal to noise ratio (SNR) can be exactly compared to the model and may be varied more systematically than a real sample.

5. Results and Discussion

5.1 Experimental Data

A metallic foam sample ($Al_{50}Ni_{25}Fe_{25}$, IFAM Bremen) has been subjected to a tomography experiment using monochromatic (E = 50 keV) synchrotron radiation (storage ring BESSY II in Berlin). The sample (cross-section app. 1.1 × 0.65 mm^2) was projected under 1200 angles of rotation in a 180° sector (corresponding to an angular increment of 0.15°). The attenuated radiation intensity was detected with a 4008 × 2672 pixel detector (pixel size: 1.1 μm). The incident beam was narrowed to the field of view by a slit system to avoid detector backlighting (Lange *et al*., 2012). In order to study missing wedge effects, a 120° sector of projections (corrected for flat-field and dark-field intensity) was used for the reconstruction. But in contrast to typical electron tomography data, the availability of the complete data set provides 180° reconstructions serving as reference. Thus, the missing wedge reconstructions can be compared to the 180° FBP under identical experimental conditions.

The DIRECTT reconstruction is performed according to the partially discrete procedure with 6 cycles at reduction factor γ = 0.2, 5 cycles at full density ρ_0, and 5 cycles without restriction.

We discuss reconstruction results at the example of a single slice and the respective Fourier transforms as displayed in Figs. 4 and 5, the 180° FBP reference a), 120° FBP b), and the 120° DIRECTT reconstruction c). The (arbitrarily chosen) mean direction of the projection sector corresponds to the horizontal axis.

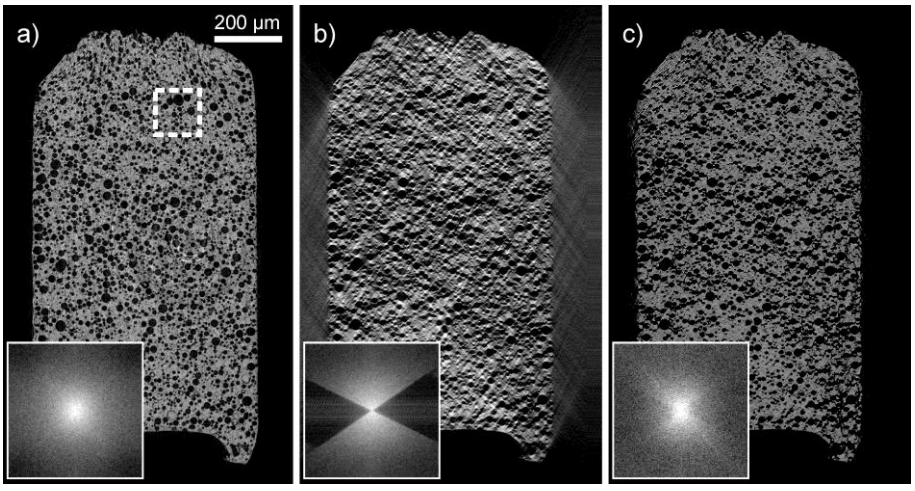

Fig. 4. Reconstruction of a single slice of the metallic foam and the respective magnitudes of Fourier transforms (insets): (a) reconstruction of the full (180°) sinogram by FBP serving as reference, (b) FBP of the 120° sinogram, (c) DIRECTT reconstruction of the 120° sinogram (11 iterations). The dashed box indicates the detail of Fig. 5.

Further details are visualised by Fig. 5. Magnified identical details of Fig.4 reveal typical differences. Density profiles along a selected single pore (arrows) indicate a pore elongation of the 120° FBP about 30 % (FWHM) while the pore width of the 120° DIRECTT image remains unchanged (Fig 5d). The polar plots of the Fourier transforms (Fig. 5e) provide the different filling of the missing wedge, with the DIRECTT case near to the 180° reference.
Closer inspection of the FBP reveals some peculiarities:

(i) Elongation artefacts, which distort the roughly circular pores to lemon-like objects, point along the mean direction of the projection sector. This involves that adjacent but separated pores (as seen in the 180° reference) seem to be connected.

(ii) In the perpendicular direction an overshooting contrast at the pore edges occurs (Fig. 5b).

(iii) Roughly 20 % of the total mass is located outside the sample area (see the cross-hatching structure to the left and right of the sample (Fig. 4b)).

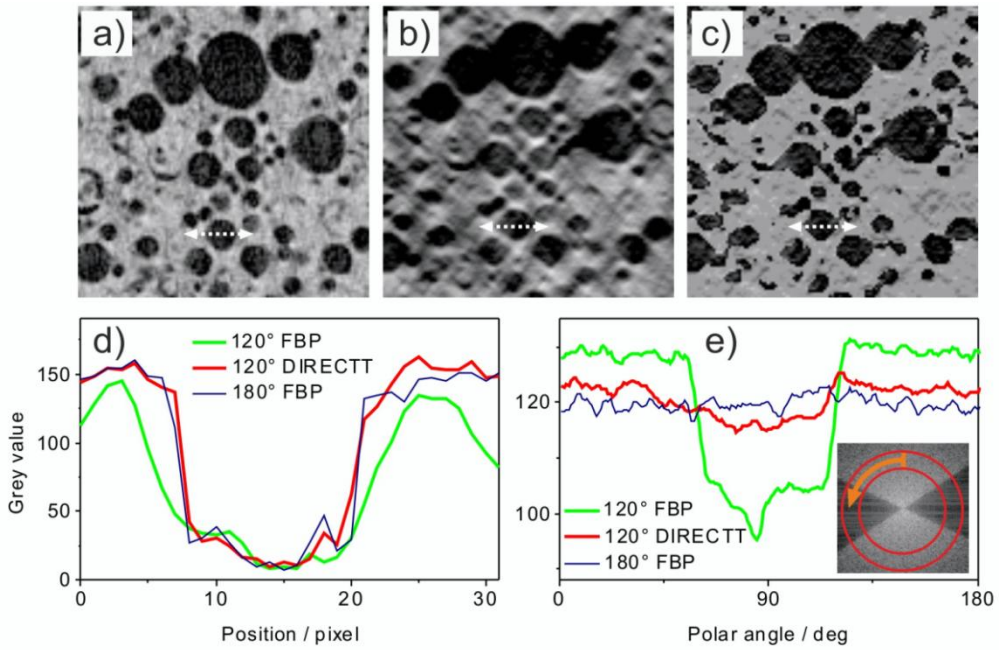

Fig. 5. Magnified identical details of the metallic foam reconstruction of Fig.4; a) 180° FBP reference, b) 120° FBP, c) 120° DIRECTT reconstructions, d) density profiles across a selected single pore (dotted arrows), e) polar plots of the respective Fourier transforms as sketched in the inset.

Application of the DIRECTT algorithm as described in section 3 reduces the listed artefacts considerably (except of minor dark vertical streak artefacts). The pore boundaries appear as closed circular objects. As demonstrated in a former study (Hentschel et al., 2010), the edge contrast of the pores is higher than in the reference by FBP and without density overshoot. The corresponding Fourier transform reflects these advantages by the partial filling of the missing wedge sectors. For the required nine iteration cycles the additional computing effort rises by a factor of nine as well.

5.2 Simulated Data

The simulated model data emulate the foam structure to a certain degree: the pores are distributed randomly and do not overlap (Fig. 6a). In contrast to the real foam, the density is strictly binary except for the pore edge pixels whose values correspond to the partial pixel coverage. Furthermore, the pore size is kept constant (mono dispersed) in the single models.

These phantoms are generated by random sequential adsorption (RSA) models (Illian *et al*., 2008). The models are realized in a 500×500 pixel window at a pore size of 20 pixels in diameter. 100 phantoms are generated, whose projections are subjected to different signal-to-noise ratios (SNR, ranging from 20 to 100, (Lück *et al*., 2010)).

In order to compare the reconstruction properties of typical model patterns Fig. 6 shows a 20 pixel pore distribution model, which was projected with angular increments of 0.5° and a MW of 60°. At a SNR of 100, the SIRT result, the filtered back projection, and the according DIRECTT result are depicted. Considering the isotropic edge reproduction of pores as the main issue of the MW problem neither FBP nor SIRT reconstructions (Fig. 6b, 6c) are convincing. However, the DIRECTT result (Fig. 6d) provides a good approximation of the individual model pores. Similar to the experimental data the dark vertical streak artefacts appear again. Currently, these artefacts are inevitable, however in terms of integral evaluation they do not disturb the angular distribution function of the more frequent pore edges, as proved by the absence of additional horizontal streaks in the FFT. Awareness is required to prevent misinterpretation as cracks.

The insets display the corresponding 2D Fourier transform magnitudes (the circular interference fringes origin from the uniformity of the pores). Comparing the reconstruction techniques, DIRECTT yields an analogous reduction of the MW as observed with the metallic foam sample (Fig. 4). The FBP and SIRT results exhibit pronounced dark missing wedge sectors (Fig. 6b and c). The DIRECTT result performs with a partially filled missing wedge area up to the fourth interference ring, corresponding to a quarter disc diameter (5 pixel resolution).

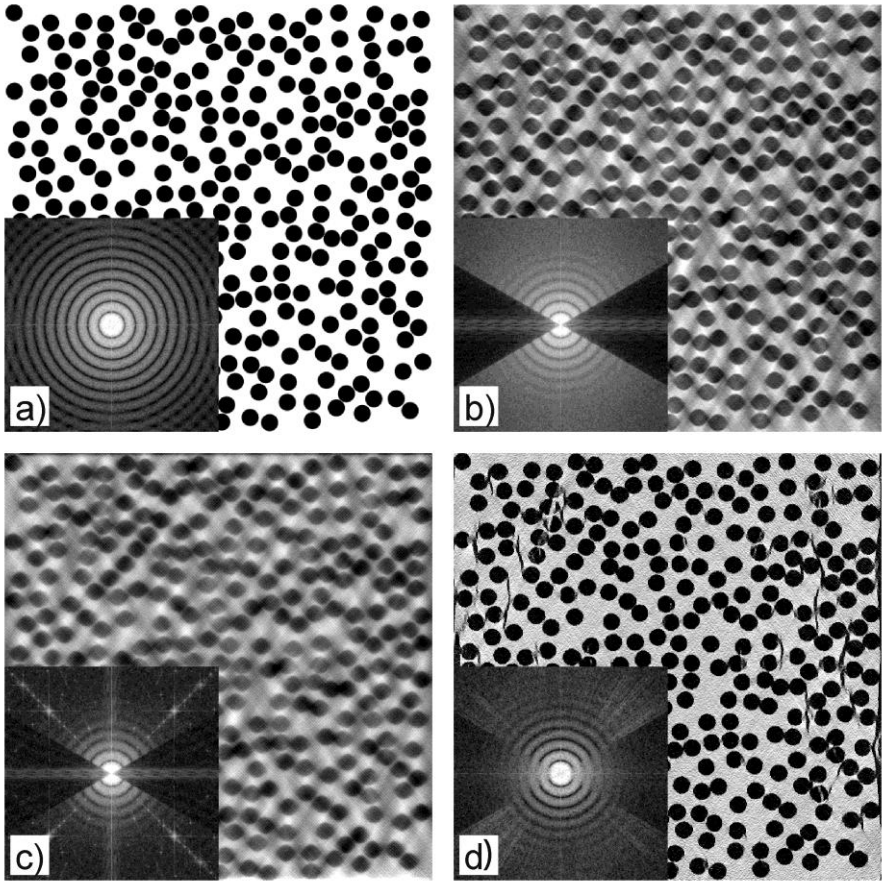

Fig. 6. 20 pixel pore model (a) and the 60° missing wedge reconstructions obtained from simulated sinograms with SNR of 100, (b) FBP, (c) SIRT, and (d) DIRECTT result (16 iterations). The respective magnitude 2D Fourier transforms of the insets reveal the different evolution of the missing wedge by the dark sectors.

For the purpose of statistical assessment of the reduction of MW artefacts the pore edges are extracted by a gradient filter and the resulting polygonal tracks are represented by Rose-of-Direction plot (RDR). The angular mismatches are evaluated by very few angles in steps of $\pi/8$ (the only discrete directions in a 3×3 pixel grid). The RDR (probability) densities of Fig. 7 show in particular that FBP and SIRT perform properly perpendicular to the mean direction (0°, horizontal direction in Fig. 6), while almost no edges are detected in the mean direction. In contrast, DIRECTT results in similar densities in both directions (isotropy: ratio near 1).

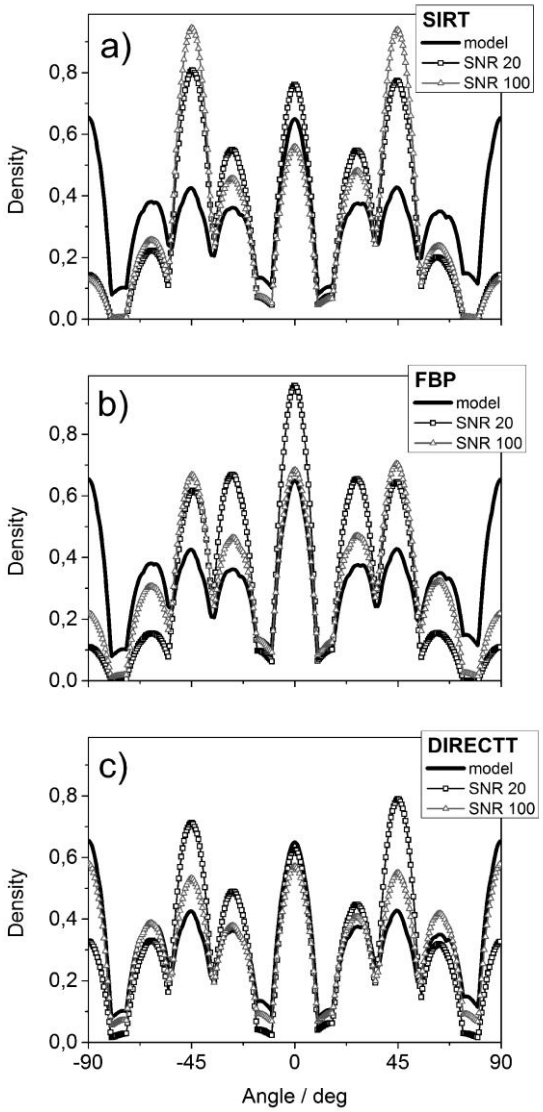

Fig. 7. Estimated (probability) densities for the rose of directions (RDR) of polygonal tracks extracted from SIRT (a), FBP (b), and DIRECTT (c) reconstructions of the simulated models for different SNR (20 and 100) under a missing wedge of 60°. The RDR of the pore boundaries in the original phantoms is plotted as bold line.

Based on such directional evaluation, Fig. 8a displays the density ratios mainly in question at 90° and 0° over different SNR. Accordingly, the L^2 distance (mean-squared error of the density estimations) between the reconstructions by the different algorithms and the model indicates the significantly smaller mismatch of DIRECTT (Fig. 8b) for all SNR examples.

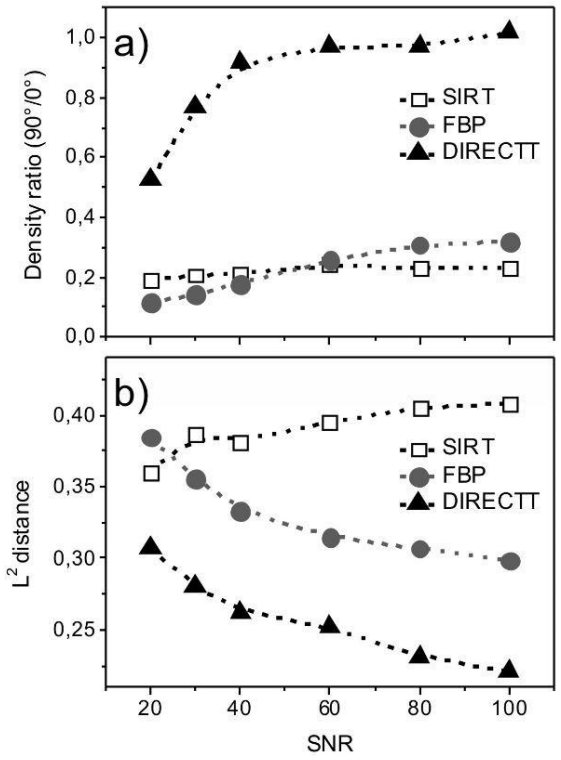

Fig. 8. Integral statistical performance of phase boundaries in missing wedge CT reconstructions by SIRT, FBP and DIRECTT; (a) ratios of RDR densities at 90° and 0°; (b) L^2-distances from the original phantoms as a function of SNR.

6. Conclusion

The application of the DIRECTT algorithm reduces the typical missing wedge artefacts. The presented strategy to suppress the artefacts by the iterative algorithm is realized by variation of reconstruction parameters in the course of iterations. The applied version of the reconstruction procedure combines elements from discrete tomography used to determine the coarse shape of objects with subsequent (non-discrete) refinements by iterations without mass restrictions. Thus, more realistic greyscale levels are obtained.

The reconstruction strategy of DIRECTT works with experimental data as well as model simulations. Visual comparison to filtered back projection reveals the advantages as well as the inspection of the wedge angle by Fourier magnitude images. It should be emphasized that the intermediate binary reconstructions are not a general requirement to cope with the missing wedge problem. However, the binary restriction reduces computing effort (i.e., the number of iteration cycles) for similar tomogram quality. It may equally be applied to discrete or non-discrete datasets but finally the suppression of the intermediate discrete levels can be controlled by histogram analysis.

For further assessment of the reconstruction quality, adapted techniques based on spatial statistics are applied to a large number of models of randomly distributed circular discs. Deviations of the RDRs between the extracted boundaries in the phantoms and the various reconstructions were assessed by the L^2-distance of the density functions. The descriptive statistical results demonstrate the quality of DIRECTT reconstructions with respect to FBP and SIRT at different noise levels. Other algorithms will be investigated for further comparisons in future work in correlation to the required computation capacities. The presented findings do not finally characterize all the potentials of the algorithm and further efforts are required for faster computation and better understanding of its limitations.

Acknowledgement

The authors gratefully acknowledge financial support of the German Federal Ministry of Education and Research (BMBF) under grant numbers 05M10DAA, 05M10VUA, and 05M10KTA. Sincere thanks are given to J. Weise (IFAM Bremen) for supply of the foam sample.

References

Arslan, I., Tong, J.R. & Midgley, P.A. (2006) Reducing the missing wedge: High-resolution dual axis tomography of inorganic materials. *Ultramicroscopy* **106**, 994-1000.
Averbuch, A., Coifman, R.R., Donoho, D.L., Israeli, M. & Shkolnisky, Y. (2008) A Framework of discrete integral transformations I – The pseudo polar Fourier transform. *SIAM J. Sci. Comput.* **30**, 764–784.
Bals, S., Batenburg, K.J., Verbeeck, J., Sijbers, J. & van Tendeloo, G. (2007) Quantitative Three-Dimensional Reconstruction of Catalyst Particles for Bamboo-like Carbon Nanotubes. *Nano Lett.* **7**, 3669–3674.
Batenburg, K.J. (2005)An evolutionary algorithm for discrete tomography. *Discrete Appl. Math.* **151**, 36-54.
Batenburg, K.J., Bals, S., Sijbers, J., Kübel, C., Midgley, P.A., Hernandez, J.C., Kaiser, U., Encina, E.R., Coronado, E.A. & van Tendeloo, G.(2009) 3D imaging of nano materials by discrete tomography. *Ultramicroscopy* **109**, 730–740.
Biermans, E., Molina, L., Batenburg, K.J., Bals, S. & van Tendeloo, G. (2010) Measuring Porosity at the Nanoscale by Quantitative Electron Tomography. *Nano Lett.* **10**, 5014–5019.
Chen, D., Goris, B., Bleichrodt, F., HeidariMezerji, H., Bals, S., Batenburg, K.J., de With, G. & Friedrich, H. (2014) The properties of SIRT, TVM, and DART for 3D imaging of tubular domains in nanocomposite thin-films and sections. *Ultramicroscopy* **147**, 137–148.
Fernandez, J.-J. (2013) Computational methods for materials characterization by electron tomography. *Curr.Opin. Solid St. M.* **17**, 93-106.
Gilbert, P. (1972) Iterative Methods for the Three-dimensional Reconstruction of an Object from Projections. *J. Theor. Biol.* **36**, 105-117.
Gordon, R., Bender, R. & Herman, G.T (1970). Algebraic Reconstruction Techniques (ART) for Three-dimensional Electron Microscopy and X-ray Photography. *J. Theor. Biol.* **29**, 471-481.
Grothausmann, R., Manke, I., Zehl, G., Dorbandt, I., Bogdanoff, P., Fiechter, S., Hentschel, M.P., Lange, A., Kupsch, A., Hilger A. & Banhart, J. (2010) Characterization of catalyst materials for fuel cells using electron tomography. *Mater. Test.* **52**, 706-711.
Grothausmann, R., Zehl, G., Manke, I., Fiechter, S., Bogdanoff, P., Dorbandt, I., Kupsch, A., Lange, A., Hentschel, M.P., Schumacher, G. & Banhart, J. (2011) Quantitative Structural Assessment of Heterogeneous Catalysts by Electron Tomography. *J. Am. Chem. Soc.* **133**, 18161-18171.
HeidariMezerji, H., van den Broek, W. & Bals, S. (2011) A practical method to determine the effective resolution in incoherent experimental electron tomography. *Ultramicroscopy* **111**, 330-336.
Hentschel, M.P., Lange, A., Kupsch, A. & Müller, B.R. (2010) Reconstruction of incomplete model data sets in computed tomography by Directt algorithm. *Mater. Test.* **52**, 668-675.
Illian, J., Penttinen, H., Stoyan, H. & Stoyan, D. (2008) Statistical Analysis and Modelling of Spatial Point Patterns, John Wiley & Sons, Chichester.
Kak, A.C. & Slaney, M. (1988) Principles of computerized tomographic imaging, IEEE Press, New York.

Kardjilov, N., Manke, I., Hilger, A., Strobl, M. & Banhart, J. (2011) Neutron imaging in materials science. *Mater. Today* **14**, 248-256.
Kawase, N., Kato, M., Nishioka, H. & Jinnai, H. (2007) Transmission electron microtomography without the "missing wedge" for quantitative structural analysis. *Ultramicroscopy* **107**, 8-15.
Kupsch, A., Lange, A., Hentschel, M.P. & Müller, B.R. (2010) Improved Computed Tomography by Variable Desmearing. *Mater. Test.* **52**, 394-400.
Lange, A. & Hentschel, M.P. (2003) patent publication DE 103 07 331 A1.
Lange, A. & Hentschel, M.P. (2006) patent publication US2006 0233459 A1.
Lange, A., Hentschel, M.P. & Schors, J. (2004) Direct iterative Reconstruction of computed tomography trajectories (DIRECTT), Proceedings of 15th WCNDT, Montreal, Canada, Aug 30 – Sept 3, 2004.
Lange, A., Hentschel, M.P. & Kupsch, A. (2008) Computed tomography reconstructions by DIRECTT: 2D model calculations compared to filtered backprojection. *Mater. Test.* **50**, 272-277.
Lange, A., Kupsch, A., Hentschel, M.P., Manke, I., Kardjilov, N., Arlt, T. & Grothausmann, R. (2011) Reconstruction of limited CT data of fuel cell components using DIRECTT. *J. Power Sources* **196**, 5293-5298.
Lange, A., Hentschel, M.P., Kupsch, A. & Müller, B.R. (2012) Numerical correction of X-ray detector backlighting. *Int. J. Mat. Res*. **103**, 174-178.
Lee, E., Fahimian, B.P., Iancu, C.V., Suloway, C., Murphy, G.E., Wright, E. R., Castaño-Díez, D., Jensen, G.J.& Miao, J. (2008) Radiation dose reduction and image enhancement in biological imaging through equally-sloped tomography. *J. Struct. Biol.* **164**, 221–227.
Lück, S., Kupsch, A., Lange, A., Hentschel, M.P. & Schmidt, V. (2010) Statistical analysis of tomographic reconstruction algorithms by morphological image characteristics. *Image Anal. Stereol.* **29**, 61-77.
Lück, S., Fichtl, A., Sailer, M., Joos, H., Brenner, R.E., Walther, P. & Schmidt, V. (2013) Statistical analysis of the intermediate filament network in cells of mesenchymal lineage by grey value-oriented segmentation methods. *Computation. Stat.* **28**, 139-160.
Manke, I., Hartnig, C., Kardjilov, N., Hilger, A., Lange, A., Kupsch, A. & Banhart, J. (2009) In-situ investigation of the water distribution in PEM fuel cells by neutron radiography and tomography. *Mater. Test.* **51**, 219-226.
Manke, I., Kardjilov, N., Schäfer, R., Hilger, A., Strobl, M., Dawson, M., Grünzweig, C., Behr, G., Hentschel, M., David, C., Kupsch, A., Lange, A. & Banhart, J. (2010) Three-dimensional imaging of magnetic domains. *Nat. Commun.* **1**, 125. (doi: 10.1038/ncomms1125).
Markötter, H., Manke, I., Kuhn, R., Arlt, T., Kardjilov, N., Hentschel, M.P., Kupsch, A., Lange, A., Hartnig, C., Scholta, J. & Banhart, J. (2012) Neutron tomographic investigations of water distributions in polymer electrolyte membrane fuel cell stacks. *J. Power Sources* **219**, 120-125.
Midgley, P.A. & Weyland, M. (2003) 3D electron microscopy in the physical sciences: the development of Z-contrast and EFTEM tomography. *Ultramicroscopy* **96**, 413–431.
Midgley, P.A. & Dunin-Borkowski, R.E. (2009) Electron tomography and holography in materials science. *Nat. Mater.* **8**, 271-280.
Penczek, P., Marko, M., Buttle, K.& Frank, J. (1995) Double-tilt electron tomography. *Ultramicroscopy* **60**, 393-410.
Radermacher, M. (1988) Three-Dimensional Reconstruction of Single Particles from Random and Nonrandom Tilt Series. *J. ElectronMicr. Tech.* **9**, 359-394.

Radon, J. (1917) Über die Bestimmung von Funktionen durch ihre Integralwerte längs gewisser Mannigfaltigkeiten. *Berichte der math.-phys. Kl. Sächsischen Gesellschaft der Wissenschaften zu Leipzig* **59**, 262-277.
Smith, S.W. (1997) The Scientist and Engineer's Guide to Digital Signal Processing, California Technical Publishing, San Diego.
Stock, S.R. (2008) Recent advances in X-ray microtomography applied to materials. *Int. Mater. Rev.* **53**,129–181.
Sidky, E.Y., Kao, C.-M.& Pan, X. (2006) Accurate image reconstruction from few-views and limited-angle data in divergent-beam CT.*J. X-ray Sci. Technol*. **14,** 119-39.
Tong, J., Arslan, I. & Midgley, P. (2006) A novel dual-axis iterative algorithm for electron tomography. *J. Struct. Biol.* **153**, 55–63.
Wolf, D., Lubk, A. & Lichte, H. (2014) Weighted simultaneous iterative reconstruction technique for single-axis tomography. *Ultramicroscopy* **136**, 15-25.
Zürner, A., Doblinger, M., Cauda, V., Wei, R. & Bein, T. (2012) Discrete tomography of demanding samples based on a modified SIRT algorithm. *Ultramicroscopy* **115**, 41-49.